

Numerical Simulation of Ship Bow Wave Breaking using DES and RANS

*Zhen Ren, Jianhua Wang and †Decheng Wan

State Key Laboratory of Ocean Engineering, School of Naval Architecture, Ocean and Civil Engineering,
Shanghai Jiao Tong University, Collaborative Innovation Center for Advanced Ship and Deep-Sea Exploration,
Shanghai 200240, China

*Presenting author: renzhen90@163.com

†Corresponding author: dcwan@sjtu.edu.cn

Abstract

The phenomena of wave breaking, known as white water, has attracted many researchers since its complex mechanism and effects on the performance of ship. The CFD solver naoe-FOAM-SJTU, is used to investigate the wave breaking phenomena of the bow wave of KCS model without sinkage and trim. In the present work, the DES and RANS turbulence model are adopted to simulate the bow wave breaking of KCS in different advance speeds, i.e. $Fr=0.26$, 0.30 , 0.35 . In the simulations, volume of fluid (VOF) is employed to capture the free surface. For the $Fr=0.26$ case, the predicted resistance and wave patterns via both turbulence models are in good agreement with the available experiment data. For the $Fr = 0.35$ case, the process of overturning and breaking of bow wave were obtained by the both turbulence models, and the scars are more visible by the DES approach. The detailed flow visualizations obtained through both turbulence models, such as wake profiles, vorticity and wave patterns, are presented to illustrate the hydrodynamic performance of high speed surface ship. The present simulations give a better understanding of the ability of both turbulence models to predict the ship bow waves breaking.

Keywords: wave breaking; KCS; free surface; OpenFOAM, RANS, DES

Introduction

Despite of the high accuracy of the resistance prediction, it is still challenging to accurately resolve the breaking wave phenomenon, which has long been recognized. Extensive experiments have been performed to try to give the physical understanding of the breaking wave mechanism and provide experimental data for CFD validation. Dong et al.^[1] conducted experimental study using particle-image-velocimetry (PIV) measurements to analyze the velocity component and vorticity distribution at $Fr=0.28$ and $Fr=0.45$. The vorticity and its associated lateral flow field are analyzed. Duncan^[2] studied the breaking and non-breaking wave resistance of a 2-D hydrofoil via the experiments in which they found the drag associated with breaking was more than 3 times the drag theoretically obtained with non-breaking waves. Kayo and Takekuma^[3] investigated bow wave breaking phenomenon around full ship models by velocity field measurements and by a flow visualization technique. They found that there was a shear flow on the free surface. Roth et al.^[4] utilized PIV to measure the flow structure and turbulence within the bow wave of DDG-51 model 5422. In the measurements, they also found that the negative vorticity originated at the toe of the wave while the positive vorticity was generated on the crest of the wave. In addition, they

discovered that the great energy losses were experienced at the toe. Longo and Stern^[5] performed mean velocity measurements using a five-hole Pitot and wave elevation measurements using capacitance wires and point gauges for the static drift condition showing the presence of a bow wave breaking induced vortex on the windward side of the model. Olivieri et al.^[6] studied the bow wave breaking of model DTMB 5415 and they analyzes the scars and vortices induced by bow and shoulder wave breaking. In that study, the large extents of plunging bow was observed at $Fr=0.35$ and spilling shoulder wave breaking was investigated.

Despite the extensive study through experiment, numerical simulation has also been adopted to predict and analyze the ship wave breaking phenomena. In the numerical simulation of Wilson et al.^[7], the unsteady single-phase level set method was adopted to resolve and investigate bow wave breaking around a surface combatant advancing in calm water, including induced vortices and free surface scars. The velocity component and vorticity distribution were in good agreement with the experiment data. Moraga et al.^[8] proposed a sub-grid model for air entrainment in the bow waves breaking and applied for the simulation of naval surface ship DTMB 5415 and Athena. The model compared favorably with data at laboratory scale and also presented the right trends at full-scale. Marrone et al.^[9] used a 2D+t SPH model to analyze the breaking wave pattern of the vessel DTMB 5365, and the overturning and breaking of bow wave were captured clearly. Marrone et al.^[10] developed a 3D SPH solver to simulate the bow wave breaking of Alliance vessels. The results achieved by the solver were compared with the experimental measurements and numerical results from RANS simulation in which the level set method was applied to resolve the free surface. Noblesse et al.^[11] reviewed the recent results about the overturning and breaking bow wave regimes, and the boundary that divides these two basic flow regimes. Questions and conjectures about the energy of breaking ship bow waves, and free-surface effects on flow circulation, are also noted.

In present work, high resolution Volume of Fluid (VOF) method is used to accurately resolve the large deformation of free surface. The main framework of this paper goes as following. The first part is the numerical methods, where DES and RANS turbulence models are presented. The second part is the geometry model and grid generation. Then comes the simulation part, where wave breaking simulations are present at different Froude numbers. In this part, extensively comparisons are performed between the results obtained via different turbulence models including ship resistance, wave patterns and wake fields at longitudinal slices. Finally, a conclusion of this paper is drawn.

Numerical methods

Governing equations

The in-house CFD solver naoe-FOAM-SJTU^[12-14], developed on open source platform OpenFOAM, is applied in this study and VOF method is used to capture free surface around the complex geometry models. The governing equations are written as a mass conservation equation and a momentum conservation equation^[15]:

$$\frac{\partial \bar{u}_i}{\partial x_i} = 0 \quad (1)$$

$$\frac{\partial \bar{u}_i}{\partial t} + \frac{\partial \bar{u}_j \bar{u}_i}{\partial x_j} = -\frac{\partial \bar{P}}{\partial x_i} + \frac{\partial}{\partial t} \left[\nu \left(\frac{\partial \bar{u}_i}{\partial x_j} + \frac{\partial \bar{u}_j}{\partial x_i} \right) \right] - \frac{\partial \tau_{ij}}{\partial x_j} \quad (2)$$

Where, ν is the molecular viscosity, τ_{ij} is the Reynolds stress tensor or subgrid-scale stress tensor. According Boussinesq hypothesis, τ_{ij} can be expressed as

$$\tau_{ij} = \frac{2}{3} \delta_{ij} k - \nu_t \left(\frac{\partial \bar{u}_i}{\partial x_j} + \frac{\partial \bar{u}_j}{\partial x_i} \right) \quad (3)$$

Turbulence Model

The SST model was proposed by Menter^[16] and is a two-equation turbulence model. SST combines the k - ϵ and k - ω models to treat the flow in the boundary layer region of the near wall with k - ω and the flow in the free shear flow region with k - ϵ . This not only preserves the ability of the k - ω model to handle the boundary conditions near the wall surface, but also avoids the insensitivity of the k - ω model to the inlet parameters in the free shear flow region. The DES model assumes the eddy viscosity ν_t is a function of turbulent kinetic energy k and specific turbulence dissipation rate ω , and strain invariant S .

$$\nu_t = \frac{a_1 k}{\max(a_1 \omega, SF_2)} \quad (4)$$

In which, the transport equations^[17] for the turbulent kinetic energy k and the specific turbulent dissipation rate ω are denoted as:

$$\frac{\partial k}{\partial t} + \frac{\partial(u_j k)}{\partial x_j} = \tilde{G} - \frac{k^{3/2}}{l_{DDES}} + \frac{\partial}{\partial x_j} \left[(v + \alpha_k \nu_t) \frac{\partial k}{\partial x_j} \right] \quad (5)$$

$$\frac{\partial \omega}{\partial t} + \frac{\partial(u_j \omega)}{\partial x_j} = \gamma S^2 - \beta \omega^2 + \frac{\partial}{\partial x_j} \left[(v + \alpha_\omega \nu_t) \frac{\partial \omega}{\partial x_j} \right] + (1 - F_1) CD_{k\omega} \quad (6)$$

The l_{DDES} in k -equation is mixing length scale which control the switch of solution between RANS and LES.

VOF method and surface tension

For the wave breaking simulations, the free surface capture method plays an important role in the accuracy of predicted results. In the present work, VOF method with bounded compression technique^[18] is applied to capture free surface and the transport equation is expressed as:

$$\frac{\partial \alpha}{\partial t} + \nabla \cdot [(\mathbf{U} - \mathbf{U}_g) \alpha] + \nabla \cdot [\mathbf{U}_r (1 - \alpha) \alpha] = 0 \quad (7)$$

Where α volume of fraction, 0 and 1 represent that the cell is filled with air and water respectively and $0 < \alpha < 1$ stands for the interface between two-phase fluids. \mathbf{U}_r in Eqn. (7) is the velocity field used to compress the interface and it only takes effect on the free surface due to the term $(1 - \alpha) \alpha$.

According to the literature concerning wave breaking, small scale wave breaking is strongly influenced by surface tension. The role played by the surface tension is quite different for breaking and non-breaking waves since the surface tension pressure jump depends on the magnitude of the radius of curvature of the free surface. In order to reappear the wave patterns of the experiment, the surface tension is taken account in the present simulation and the surface tension is expressed as:

$$f_\sigma = \sigma \kappa \nabla \alpha \quad (8)$$

Where σ stands for the surface tension, κ is the curvature of free surface and it is defined as:

$$\kappa = -\nabla \cdot \mathbf{n} = -\frac{\sum_f \mathbf{S}_f \cdot \mathbf{n}_f}{V_i} \quad (9)$$

V_i represents the volume of cell i , $\sum_f S_f$ stands for the sum of value on each face of cell.

Geometry model and grid generation

Geometry model

As a full-formed hull, the wave breaking of KRISO Container Ship (KCS) has aroused significant interest of researchers. The geometry model that is the 6.0702 m replica with rudder in numerical simulations is shown in Fig. 1, and its principle parameters are listed in Table 1. Extensive experiments have been conducted for the ship model under various Froude numbers except for Fr above 0.30. But the phenomena of wave breaking of KCS will be observed clearly at Fr=0.35 according to the previous work in which the study of the effects of different speeds on the wave breaking are carried out. In the present work, the wave breaking simulations of KCS at Fr= 0.35 are conducted. In the numerical simulation, the model is fixed without the sinkage and trim.



Fig. 1 Geometry model of KCS (Case 2.10)

Table 1 Principle dimensions of KCS

Main particulars		Full scale	Model scale
Length between perpendiculars	L_{pp} (m)	230	6.0702
Maximum beam of waterline	B_{WL} (m)	32.2	0.8498
Draft	T (m)	10.8	0.2850
Displacement volume	Δ (m ³)	52030	0.9565
Wetted surface area (with rudder)	S_0 (m ²)	9645	6.7182

Grid Generation

Due to the high computational costs and fixed ship model condition, only half of the computational domain is adopted for the numerical simulations. Fig. 2 shows the computational domain and the boundary conditions.

All-hexahedral unstructured grid adopted in the present simulations is generated by the software, *Hexpress*. The grid number in x, y, z direction is $100 \times 30 \times 45$, respectively. To better resolve the bow wave breaking and free surface wave pattern, several blocks are adopted to refine the regions around the hull, bow and local free surface, as shown in Fig. 3. Block 1 is the region that wraps the hull surface. The 18.3 million grid scheme is obtained via the refinement in several blocks, as listed in Table 2. The scale of the size of the highest-level refinement region to L_{pp} is about $1.56e-3$. Fig. 4 presents the global and local profile of grid distribution.

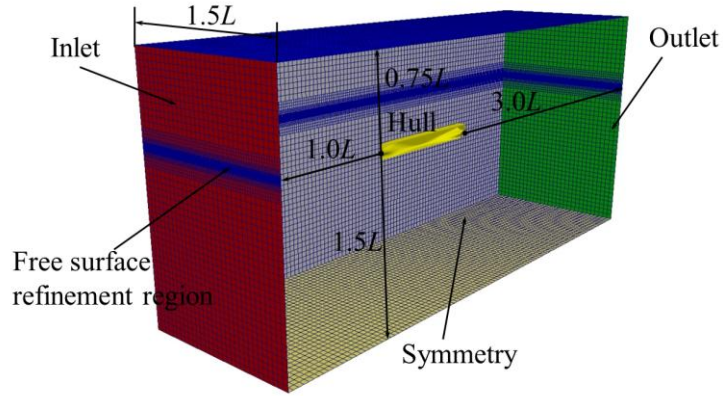


Fig. 2 Domain and boundary conditions.

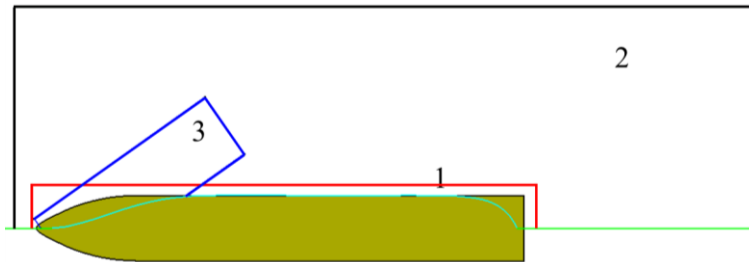


Fig. 3 Refinement regions.

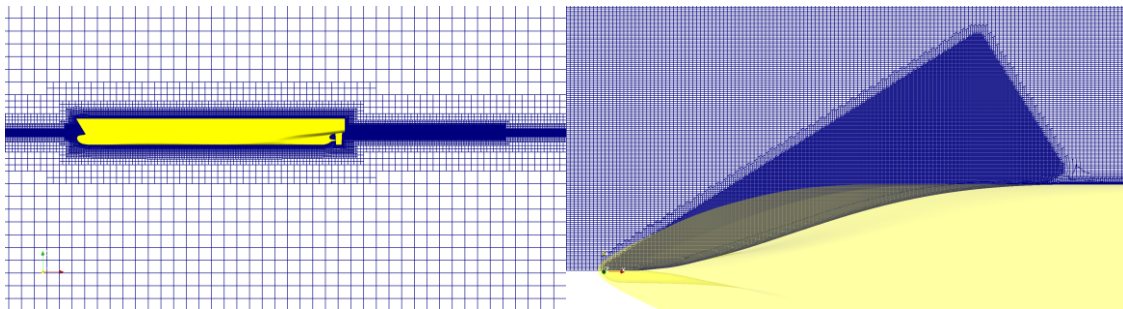


Fig. 4 Profile of grid distribution, global (left), local grid of bow (right)

Table 2 Grid refinement strategy

Total	No.	Refinement level (x, y, z)	Ratio($/L_{pp}$) ($\times 10^{-3}$)
	1	$3 \times 3 \times 3$	$6.25 \times 6.25 \times 6.25$
18.3Million	2	$4 \times 4 \times 5$	$3.125 \times 3.125 \times 1.5625$
	3	$5 \times 5 \times 5$	$1.5625 \times 1.5625 \times 1.5625$

Analysis of simulation results

Validation of Numerical Scheme

The focus of the present study is on the resolution of bow wave breaking of KCS via DES and RANS at different speeds, i.e. $Fr = 0.26, 0.30, 0.35$. The sinkage and trim of the hull is not taken into consideration in order to simplify the numerical simulation. The condition at $Fr = 0.26$ is selected to validate the prediction accuracy of the current numerical scheme.

Table 3 Comparison of experimental and predicted resistance

Parameters	EFD	CFD	
		RANS	DES
U (m/s)	2.017	2.017	2.017
Sinkage (/Lpp)	-2.074e-3	None	None
Trim (deg)	-0.1646	None	None
Wetted surface area with rudder	6.6978	6.7449	6.7449
$C_t(\times 10^3)$	3.835	3.662	3.644
Error		-4.51%	-4.98%

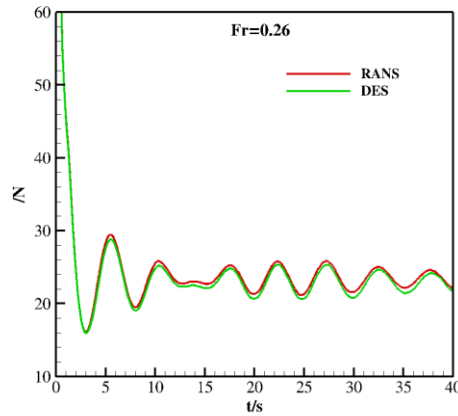


Fig. 5 Comparison of resistance obtain at $Fr=0.26$ via DES and RANS

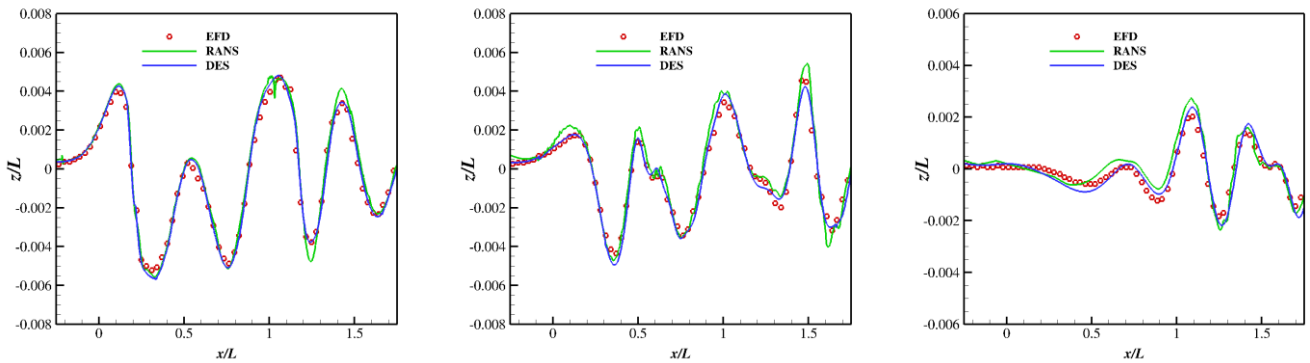


Fig. 6 Comparison of free-surface between experiments (circles) and computational results (green: RANS; blue: DES) at different cutting planes.

Fig. 5 shows the time history of total resistance via both turbulence models. As we can see, the convergence trends of total resistance via both numerical schemes are consistent. Table 3 shows the comparison between the predicted resistance and the experiment data. The errors via RANS and DES turbulence model are about -4.51% and -4.98%, respectively. Since the ignorance of the hull posture, the errors of resistance are acceptable. **Fig. 6** shows the wave height of the three profiles ($y/L = 0.0741, 0.1509, 0.4224$), obtained by experiment and both numerical simulations schemes. From the near field to the far field, the calculated free surface via both numerical schemes are consistent with the experimental measurements. Compared with the results via RANS schemes, the results via DES scheme is slightly better agreement with the experiment data. The results show that the numerical scheme that DES turbulence

model may be more suitable to simulate for capturing the free surface. On the other hand, the above results prove that the numerical scheme in the present work are reliable and robust.

Simulation results at $Fr=0.35$

According to the simulation results, the bow wave breaking is observed at $Fr=0.35$, so the numerical results at $Fr=0.30$ is not shown here. In the simulation of bow wave breaking of KCS at high speed, the hull also is fixed without trim and sinkage.

The time history of resistance at $Fr=0.35$ via both numerical schemes are shown in Fig. 7. The convergence trends of both lines are consistent and almost same basically. The total resistance coefficients achieved via both numerical schemes are compared in Table 4. The relative error of both resistances is 0.354% demonstrates the results via the present numerical schemes are reliable and robust.

Table 4 Comparison of resistance via DES and RANS

Parameter	$U(\text{m/s})$	Sinkage ($/L_{pp}$)	Trim (deg)	$C_t (\times 10^3)$	
				RANS	DES
Value	2.701	None	None	5.084	5.066

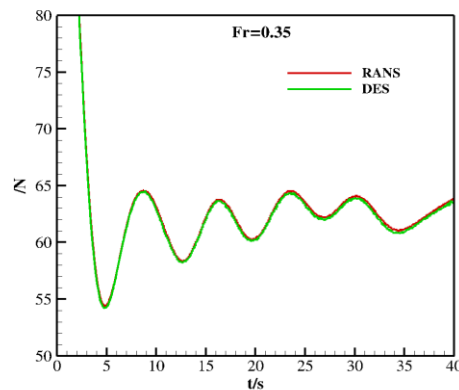


Fig. 7 Time history of total resistance via DES and RANS

The wave patterns of free surface via both turbulence models are presented in Fig. 8. As depicted in Fig. 8(a), the global profiles are same basically except bow wave. The result obtained via RANS approach is smoother than that obtained via DES approach. There are more stripes near the hull in the results achieved by the DES turbulence model. Near the bow, four scars are observed by DES method while there is only scar achieved by RANS method, as shown in Fig. 8 (b).

In the both numerical simulation, the marked difference is observed in the evolution of bow wave. Fig. 9 shows the difference between both simulation results more clearly. In the results of DES scheme, the nearest scar that is formed by the first overturning of bow wave starts at $x/L=0.09$ and disappears at $x/L=0.22$. When the bow wave plunges into the below free surface secondly, the second scar is formed at $x/L=0.16$ and it disappears at $x/L=0.28$. The third scar is also observed clearly between $x/L=0.21$ and $x/L=0.30$. The farthest scar is not visible apparently and it starts at $x/L=0.25$ and vanishes at $x/L=0.34$. Through the RANS scheme, the only one scar that starts at $x/L=0.09$ and vanishes at $x/L=0.19$ is visible clearly.

While the abrupt change and breaking of bow wave is very obvious near $x/L=0.21$ and the bow wave captured in the DES scheme seems to have better continuity and smoothness.

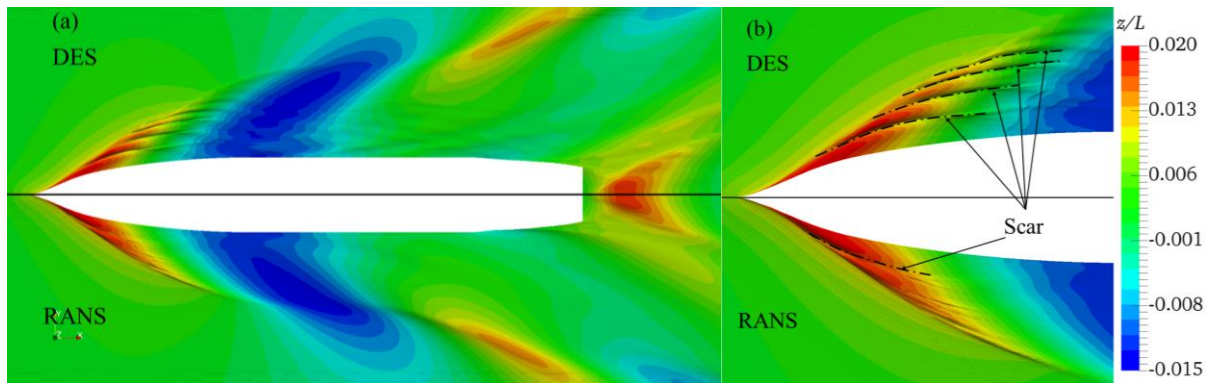


Fig. 8 Comparison of free surface via RANS (below) and DES (top), a: global profile, b: local profile

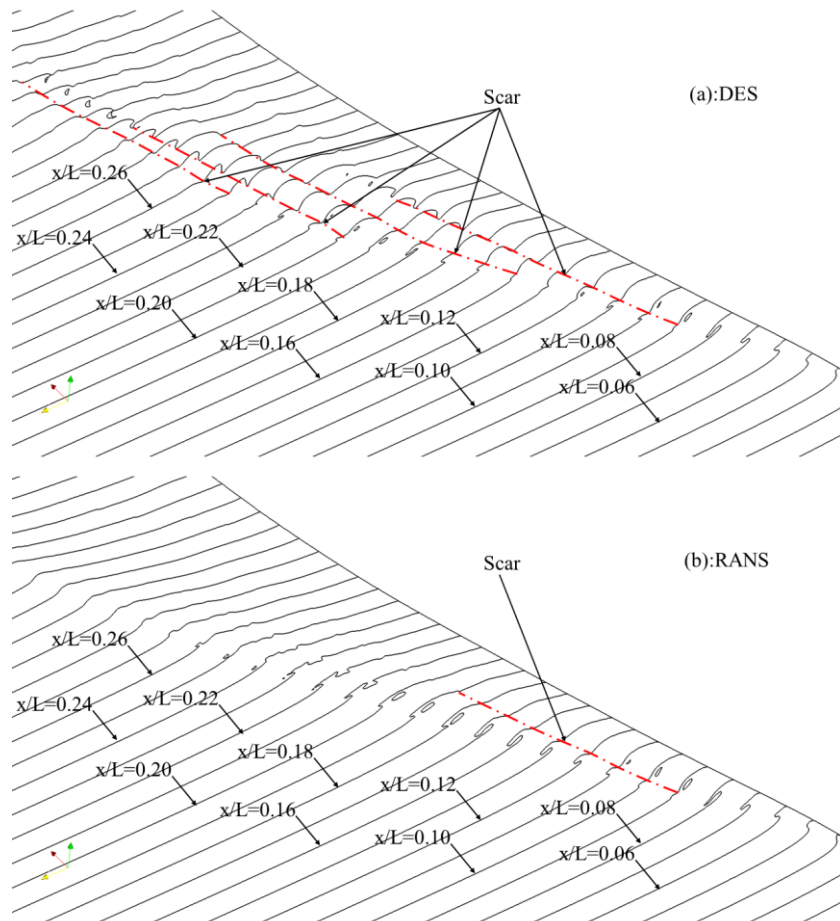


Fig. 9 Scar in bow wave breaking (a: DES, b: RANS)

The general view of the vertical structure at $Fr=0.35$, is given in Fig. 10 which presents an isosurface of the dimensionless value $Q=10$ ($Q = (S^2 + \Omega^2)/2$, S and Ω being the symmetric and antisymmetric component of velocity) colored by the velocity. With the DES approach, three vortices near the bow are visible clearly and maintained until the middle of the hull. Except the three main vortices, some fragmented vortices occur near the bow wave. The main vortices vanish near the middle of the hull. On the other hand, some larger vortices also

appear near the middle of the hull. Through the RANS approach, some small intermittent vortices are yielded and these vortices vanish rapidly in the wake.

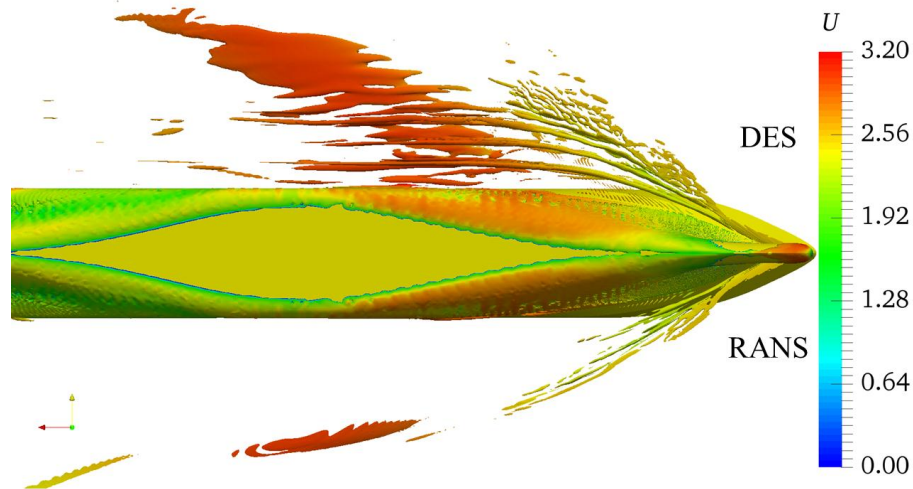


Fig. 10 Vortical structure (top: DES, below: RANS)

In order to compare the evolution of vortices more clearly, the axial vorticity distribution at different cutting planes are presented in Fig. 11. At $x/L=0.05$, the axial vorticity distribution obtained by both numerical schemes are similar. At the tip of the initial plunger, the axial vorticity is positive while the negative vorticity occurs at the high curvature region of the overturning bow wave. At $x/L=0.07$, the initial plunger generated due to the gravitational and inertial forces develops outboard and is going to reconnect with the free surface below. Although the axial vorticity distribution of both models are similar, the initial plunger yielded by DES model is thicker than that yielded by RANS approach. In addition, the initial plunger obtained by RANS scheme has shown the indication of breaking. Axial vorticity distribution is significantly different at $x/L=0.14$. The scar yielded by DES approach is clearer than that captured by RANS scheme. In the simulation of DES model, the shape of plungers is not observed while the second plunger is visible clearly in the prediction of RANS approach. In addition, the negative vorticity obtained by DES approach is much larger than that achieved by RANS scheme. In the simulation of DES model, the positive vorticity is much larger than the other scheme and concentrated on the free surface. A counter-rotating vortex pair is generated near the scar and the vortex pair pumps fluid outboard.

Though the comparison of vorticity, the vorticity yielded by both numerical schemes at $x/L=0.14$ differs greatly. In order to analyze the mechanism of bow wave, the wake field at $x/L=0.14$ is presented in Fig. 12. In the axial direction, the velocity distributions from both numerical schemes are similar. The variation of axial velocity is concentrated near the bow wave. The lowest axial velocity occurs near the wave crest and it increases with increasing distance from the hull. The obvious difference mainly due to the wave pattern is concentrated near the second plunger. Similar to the axial velocity distribution, the variation of lateral velocity is also concentrated near the bow wave. The highest lateral velocity occurs near the free surface. And the lateral velocity decreases with increasing distance from the model. The vertical velocity shows the obvious difference. The significant variation occurs near the free surface. Positive and negative vertical velocity appear alternately in the simulation of DES model leads to the counter-rotating flow so that the counter-rotating vortex pair is generated near the scar. The result obtained by the RANS approach also has this trend but it is not very clear.

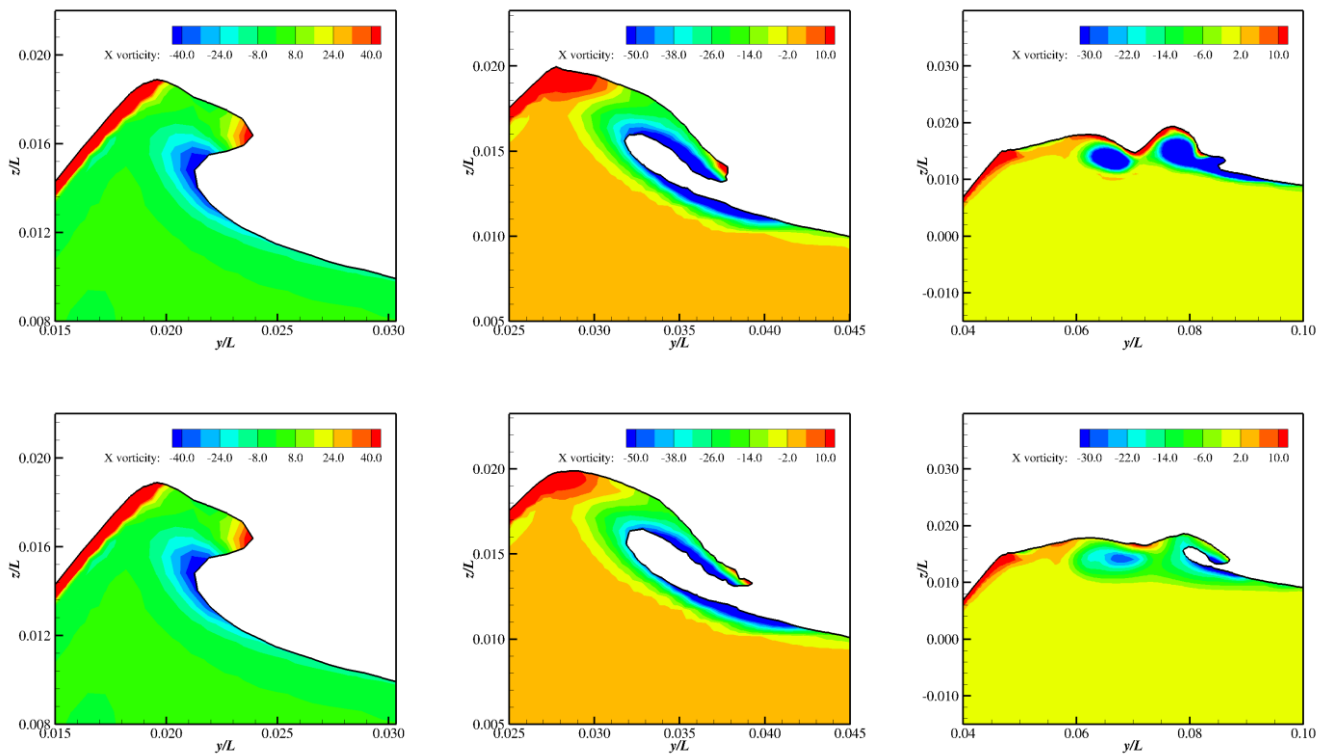


Fig. 11 Axial vorticity distribution at $x/L=0.05$ (left), 0.07 (middle) and 0.14 (right) (top: DES, below: RANS)

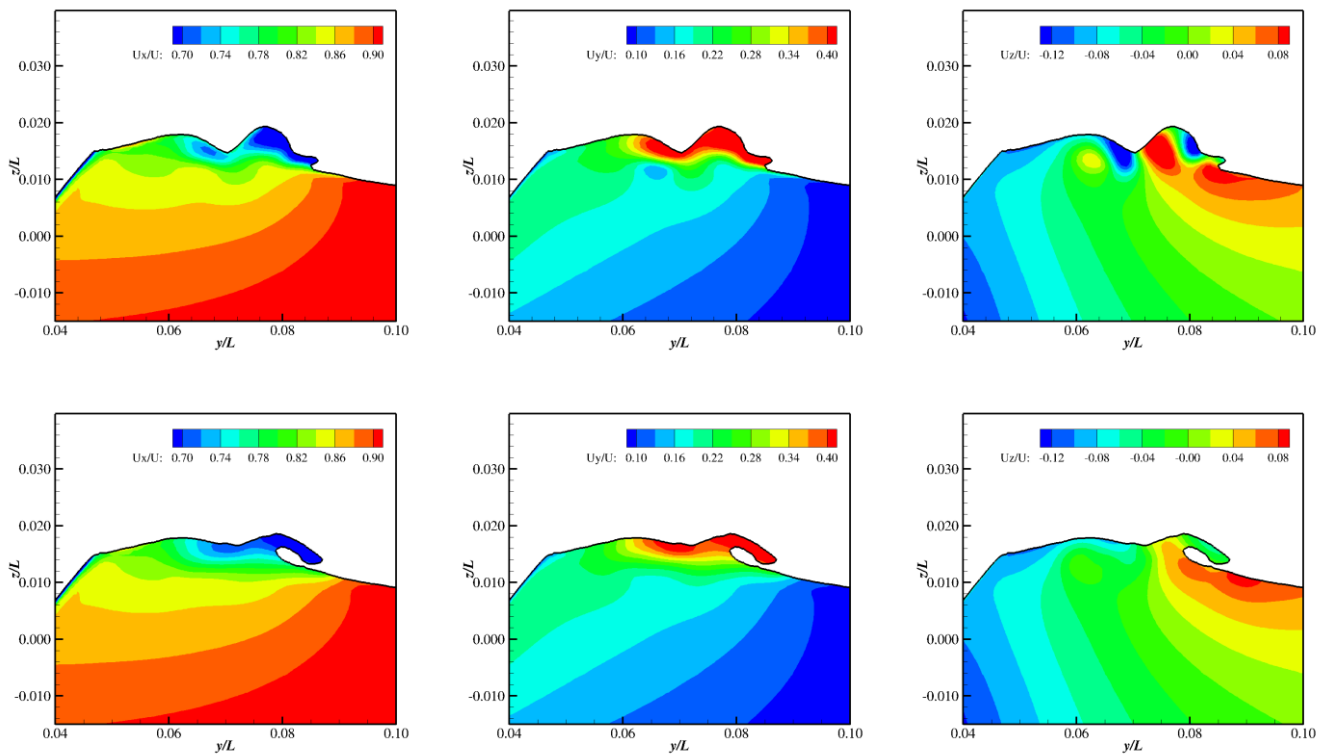


Fig. 12 Wake field distribution at $x/L=0.14$ (top: DES, below: RANS)

Conclusion

In the present study, both turbulence models, DES and RANS, are adopted to simulate the bow wave breaking of KCS. At low speed, $Fr=0.26$, in terms of resistance, the predicted result of RANS approach is slightly more accurate than DES model. While the prediction of wave pattern obtained by the latter is slightly better agreement with experiment dat. At high speed, $Fr=0.35$, the resistance achieved by both turbulence models are almost same basically. Though four scars are captured by the DES model, while only one scar is observed via RANS approach. In terms of the 3D vortical structure, DES model yields three main vortices and more fragmented vortices near the bow and the main vortices vanishes until the mid-ship, while RANS approach captures some intermittent vortices that vanish rapidly in the wake. At the cutting planes, $x/L=0.05, 0.07$, the axial vorticity distribution obtained by both numerical schemes are similar. At $x/L=0.14$, the negative vorticity obtained by DES approach is much larger than that achieved by RANS scheme. A counter-rotating vortex pair, which induces the scar, is generated near the free surface. In the wake field, the axial and lateral velocity do not present significant difference. In the results of DES method, positive and negative velocity appear alternately in the vertical direction, while RANS approach only provides a fuzzy distribution for this trend. In the future work, some small scale features, such as air entrainment, capillary wave, should be paid more attention.

Acknowledgements

This work is supported by the National Natural Science Foundation of China (51379125, 51490675, 11432009, 51579145, 11272120), Chang Jiang Scholars Program (T2014099), Program for Professor of Special Appointment (Eastern Scholar) at Shanghai Institutions of Higher Learning (2013022), Innovative Special Project of Numerical Tank of Ministry of Industry and Information Technology of China (2016-23) and Lloyd's Register Foundation for doctoral students, to which the authors are most grateful.

References

- [1] Dong, R.R., Katz, J., and Huang, T.T. (1997) On the structure of bow waves on a ship model, *Journal of Fluid Mechanics* 346, 77–115.
- [2] Duncan, J.H. (1983) The breaking and non-breaking wave resistance of a two-dimensional hydrofoil, *Journal of Fluid Mechanics* 126, 507–520.
- [3] Kayo, Y., and Takekuma, K. (1981) On the Free-Surface Shear Flow related to Bow Wave-Breaking of Full Ship Models, *Journal of the Society of Naval Architects of Japan* 149, 11–20.
- [4] Roth, G.I., Mascenik, D.T., and Katz, J. (1999) Measurements of the flow structure and turbulence within a ship bow wave, *Physics of Fluids* 11(11), 3512–3523.
- [5] Longo, J., and Stern, F. (2002) Effects of drift angle on model ship flow, *Experiments in Fluids* 32(5), 558–569.
- [6] Olivieri, A., Pistani, F., Wilson, R., Campana, E.F., and Stern, F. (2007) Scars and Vortices Induced by Ship Bow and Shoulder Wave Breaking, *Journal of Fluids Engineering* 129(11), 1445–1459.
- [7] Wilson, R.V., Carrica, P.M., and Stern, F. (2006) URANS simulations for a high-speed transom stern ship with breaking waves, *International Journal of Computational Fluid Dynamics* 20(2), 105–125.
- [8] Moraga, F.J., Carrica, P.M., Drew, D.A., and Lahey, R.T. (2008) A sub-grid air entrainment model for breaking bow waves and naval surface ships, *Computers & Fluids* 37(3), 281–298.

- [9] Marrone, S., Colagrossi, A., Antuono, M., Lugni, C., and Tulin, M.P. (2011) A 2D+t SPH model to study the breaking wave pattern generated by fast ships, *Journal of Fluids and Structures* 27(8), 1199–1215.
- [10] Marrone, S., Bouscasse, B., Colagrossi, A., and Antuono, M. (2012) Study of ship wave breaking patterns using 3D parallel SPH simulations, *Computers & Fluids* 69, 54–66.
- [11] Noblesse, F., Delhommeau, G., Liu, H., Wan, D., and Yang, C. (2013) Ship bow waves, *Journal of Hydrodynamics, Ser B* 25(4), 491–501.
- [12] Shen, Z., Cao, H., Ye, H., and Wan, D. (2012) The manual of CFD solver for ship and ocean engineering flows: naoe-FOAM-SJTU, Shanghai Jiao Tong University.
- [13] Cao, H., and Wan, D. (2014) Development of Multidirectional Nonlinear Numerical Wave Tank by naoe-FOAM-SJTU Solver, *International Journal of Ocean System Engineering* 4(1), 52–59.
- [14] Shen, Z., Wan, D., and Carrica, P.M. (2015) Dynamic overset grids in OpenFOAM with application to KCS self-propulsion and maneuvering, *Ocean Engineering* 108, 287–306.
- [15] Zhao, W., Wan, D. (2017) CFD study of VIM of a paired- column semi-submersible platform, *Proceeding of 27th International Ocean and Polar Engineering Conference*. California, USA, June 25-30, 2017, 693-700.
- [16] Menter, F. R., Kuntz, M., Langtry, R. (2003) “Ten years of industrial experience with the SST turbulence model, *Turbulence*,” *Heat and Mass Transfer* 4, 625-632.
- [17] Zhao, W., Wan, D. (2016) Numerical study of 3D flow past a circular cylinder at subcritical Reynolds number using SST-DES and SST-URANS, *Chinese Journal of Hydrodynamics*, 31(1), 1-8.
- [18] Weller, H.G. (2008) A new approach to VOF-based interface capturing methods for incompressible and compressible flow, OpenCFD Ltd, Report TR/HGW/04.